Nuclear Instruments and Methods in Physics Research B 319 (2014) 154–167

Contents lists available at ScienceDirect

Nuclear Instruments and Methods in Physics Research B

journal homepage: www.elsevier.com/locate/nimb

Shielding data for hadron-therapy ion accelerators: Attenuation of secondary radiation in concrete

S. Agosteo [a], A. Mereghetti [b,c], E. Sagia [b,d], M. Silari [b,*]

[a] Polytechnic of Milano, Department of Energy, Via Ponzio 34/3, 20133 Milano, Italy
[b] CERN, 1211 Geneva 23, Switzerland
[c] University of Manchester, Physics and Astronomy Department, Brunswick Street, Manchester M13 9PL, UK
[d] Physics Department, National Technical University of Athens, 9 Heroon Polytechniou, GR 157 80 Athens, Greece

ARTICLE INFO

Article history:
Received 17 June 2013
Received in revised form 13 October 2013
Available online 9 November 2013

Keywords:
Accelerator shielding
Particle therapy
Attenuation length
Source term
Neutron double differential distributions
Monte Carlo simulations

ABSTRACT

The secondary radiation field produced by seven different ion species (from hydrogen to nitrogen), impinging onto thick targets made of either iron or ICRU tissue, was simulated with the FLUKA Monte Carlo code, and transported through thick concrete shields: the ambient dose equivalent was estimated and shielding parameters evaluated. The energy for each ion beam was set in order to reach a maximum penetration in ICRU tissue of 290 mm (equivalent to the therapeutic range of 430 MeV/amu carbon ions). Source terms and attenuation lengths are given as a function of emission angle and ion species, along with fits to the Monte Carlo data, for shallow depth and deep penetration in the shield. Trends of source terms and attenuation lengths as a function of neutron emission angle and ion species impinging on target are discussed. A comparison of double differential distributions of neutrons with results from similar simulation works reported in the literature is also included. The aim of this work is to provide shielding data for the design of future light-ion radiation therapy facilities.

1. Introduction

A growing number of proton accelerators with energies typically up to 250 MeV are being installed in hospitals worldwide for cancer radiation therapy, exploiting the better dose distributions allowed by protons over photons and electrons. Hadrons heavier than protons can further improve precision and effectiveness of the treatment: on the one hand, the sharper Bragg peak and the lower lateral scattering allow even better sparing of healthy tissues; on the other hand, their higher relative biological effectiveness (RBE) increases the radiation response of a certain class of tumours (see e.g. Ref. [1]). At present a few medical facilities using carbon ions up to 430 MeV/amu are operational or at the planning stage, and it cannot be excluded that the use of other light ions will be investigated for future clinical use (hadron therapy) [2,3].

The radiation field which dictates the shielding requirements at hadron accelerators is dominated by the secondary neutrons produced by the interaction of the beam with the structures of the accelerator, of the beam transfer lines, of the beam delivery system (such as collimators and field-shaping devices), and with the patient himself, where the beam is ultimately lost [4]. Ducts and mazes should also be designed mainly to attenuate neutron streaming through them (see, for example, Refs. [5,6]). In spite of the growing interest in intermediate-energy ion accelerators, there are not so many shielding data available in the literature except for protons. The aim of this paper is to provide an extensive set of computational data for concrete for shielding light ion (up to nitrogen) accelerators, complementing existing data for protons [7,8] and other ions [9–12], in order to anticipate possible needs for the design of future light-ion radiation therapy facilities.

In the present work, the attenuation through concrete of the total dose equivalent produced by several ion beams impinging on thick iron and ICRU tissue equivalent targets was calculated with the FLUKA Monte Carlo code [13,14]. The calculations reproduce the dominant secondary radiation field created by the beam impacting on the target. Iron is chosen as representative of other materials of similar density and atomic number, such as copper and stainless steel, main constituents of accelerator components; tissue is chosen to represent the patient. The dose equivalent behind the shield includes contribution from all particles emitted by the target over the entire solid angle, as well as secondary particles produced in the concrete shield itself. The results of the calculations were fitted by the classical two-parameter formula of a point-source line-of-sight model. Neutron yields and energy spectra produced by the impact of the selected ions on the chosen targets were calculated. The results are compared with available literature data and discrepancies explained. The complete set of

* Corresponding author. Tel.: +41 22 7673937; fax: +41 22 7668434.
E-mail address: marco.silari@cern.ch (M. Silari).

http://dx.doi.org/10.1016/j.nimb.2013.10.015
0168-583X/

source terms and attenuation length data, specifically conceived to be directly employed in shielding calculations, are given in Appendix B. The full results (neutron energy spectra for all combinations of ion species and targets, attenuation curves and respective fits, plots showing the variation of the source terms and attenuation lengths as a function of the scoring angular bin and of the atomic number of the impinging ion Z_{ion}) can be found in Ref. [15].

2. Monte Carlo simulations

The simulations were performed with the version 2011.2 of the FLUKA Monte Carlo code [13,14]. Secondary particles produced by a mono-energetic "pencil" ion beam impinging on a thick target and emitted over the entire solid angle were transported through a large, spherical, concrete shield. The ambient dose equivalent was estimated online, folding the particle fluence with built-in fluence-to-dose equivalent conversion coefficients [16,17], provided in the FLUKA code. The energy of each ion beam was chosen in order to reach a maximum penetration in ICRU tissue of 290 mm, corresponding to the range of 430 MeV/amu carbon ions. The SRIM code [18] was used to set the ion energies. Fully stripped ions were simulated as primary beam. Table 1 lists the chosen ions and their energies.

The target was cylindrical, coaxial with the incoming beam, and slightly thicker than the ion range at the given energy for the given material: 60 mm for the iron target, 350 mm for the tissue target. Table 2 gives the elemental composition of the ICRU tissue [19] used in the simulations. The geometry of a right cylinder (i.e. diameter equal to the length) was adopted because it ensures a sufficiently conservative combination between neutron yield and spectrum hardness [4,7]. In general, shielding data for thin targets are conservative, since the emitted neutron spectrum is harder and thus more penetrating, with no self-absorption in the target itself. In contrast, the secondary particle yield is higher for a thick target, featured by a more intense low-energy component. In real situations the beam is usually lost in a rather thick target (e.g. a magnet or a collimator) and thick-target data should normally be used [5].

As done in various previous studies [4,7,8,10,11,20], the target was located at the centre of a large spherical shield made of ordinary concrete (type TFS 5.5 [21], Table 3), the inner radius of which was sufficiently large (90 m) to ensure that curvature-related effects are negligible (Fig. 1). The volume of the cavity delimited by the inner surface of the shield was "filled" with vacuum.

The particle fluence was scored by means of inverse cosine-weighted boundary crossing estimators (i.e. fluence across a surface) at different depths inside the shield, taking into account only particles directed outwards ("one-way" scoring option) [4,7,8]. Profiting from the cylindrical symmetry of the problem, the entire solid angle was divided into 12 planar angular bins, each 15° wide; angles are defined with respect to the incident beam direction. A special routine (described in Appendix A) was written and linked to FLUKA, checking the farthest scoring surface reached by any tracked particle, and triggering the scoring only when the particle was traversing it for the first time. This routine was implemented to avoid overestimating the fluence by scoring neutrons scattering back and forth across a boundary estimator, typical when scoring inside a homogeneous medium but not occurring while scoring at the boundary between the shield and the air outside it. Consequently, it was possible to score the dose inside the medium as if any given scoring surface was the outermost one. It was thus possible to run one single simulation for each selected ion-target pair for all shielding thicknesses, saving considerable computing time.

Variance reduction techniques were used, namely "geometry splitting" and "Russian roulette": each region was attributed an importance, increasing with the distance from the target, so as to maintain the fluence of particles approximately constant throughout the shield [4,7,8]. Biasing is a key ingredient for the convergence of results over a reasonable time-scale, especially in the case of deep penetration problems, and for emission directions far from the beam direction. Preliminary simulations were performed in order to reasonably tune the biasing throughout the shield for the various cases. For all ions but protons, the iron target was chosen since its spectrum is slightly harder than the one from tissue: biasing was thus tuned for the case of the iron target,

Table 1
List of ions and corresponding energies considered in the present work.

Ion beam	Charge state	Energy (MeV/amu)
^{1}H	+1	215
^{4}He	+2	223
^{7}Li	+3	250
^{9}Be	+4	286
^{11}B	+5	342
^{12}C	+6	430
^{14}N	+7	469

Table 2
ICRU four-elemental composition (per cent by weight) and density.

	H	C	N	O
ICRU	10.1	11.1	2.6	76.2
Density (g cm^{-3})	1			

Table 3
Elemental composition of concrete TSF – 5.5 [21]. The nominal water content is 5.5% and the density is 2.31 g cm^{-3}.

Elemental composition (10^{21} atoms cm^{-3}) of concrete TSF – 5.5							
H	C	O	Mg	Al	Si	Ca	Fe
8.5	20.2	35.5	1.86	0.6	1.7	11.3	0.19

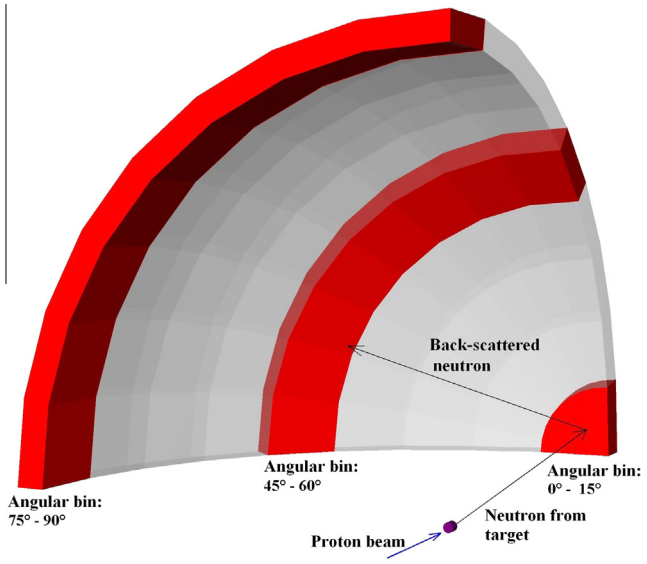

Fig. 1. FLUKA geometry plotted with SimpleGeo [22] showing the target, hit by the beam, located at the centre of the spherical shield, 90 m in radius, made of ordinary concrete. Only one octant of the 4π shield is shown. Three of the scoring angular bins (15° wide) are shown. The neutron "cross-talk" mentioned in Section 3.2, which represents the neutron transport in one angular bin after being back-scattered from another angular bin, is also sketched.

whereas it was slightly undercompensating in the case of the tissue target.

3. Results

3.1. Energy and angular distributions of source neutrons

As representative examples of the FLUKA simulation results, the energy distributions of source neutrons in the forward and backward directions for 215 MeV protons and 469 MeV/amu nitrogen ions on iron and tissue targets are shown in Figs. 2–5. The shape of the energy distributions for the other ions is similar, with the high-energy peak moving to higher energy with increasing energy per nucleon of the bombarding ion. All spectra can be found in Ref. [15]. These are results of simulations with no concrete shielding around the target, thus representing a pure target yield, not influenced by the neutron backscattering from the inner surface of the shield. Table 4 gives the total secondary neutron yield for both targets. For all ions, neutron spectra generated from the tissue target include a peculiar low energy component that is absent in the spectra generated from the iron target. This is due to the fact that the tissue target is much bigger (in both longitudinal and transverse directions) than the iron target, so that neutrons have a much higher probability to interact within the target before leaving it. Moreover, being a material with lower average atomic number, tissue is also much more effective than iron in slowing down intermediate energy neutrons. Finally, there is a clear trend of increasing neutron multiplicity with increasing atomic number of the bombarding ion, Z_{ion}.

3.2. Shielding parameters

As an example, the attenuation curves of the total ambient dose equivalent (mostly due to neutrons with some minor contribution from photons, electrons, positrons and protons) for both targets at four representative neutron emission angles (0–15°, 45–60°, 75–90° and 165–180°) are shown for 469 MeV/amu nitrogen ions in Figs. 6 and 7. The curves for the other ions show a similar behaviour [15]. For all ions, the statistical uncertainties of the Monte Carlo data are rather low (smaller than the size of the symbols in Figs. 6 and 7). The statistical uncertainties are less than 15% for all beams and targets for thicknesses up to 6 m, for the angular bins up to 120°. The uncertainties are around 15% for the angular bin

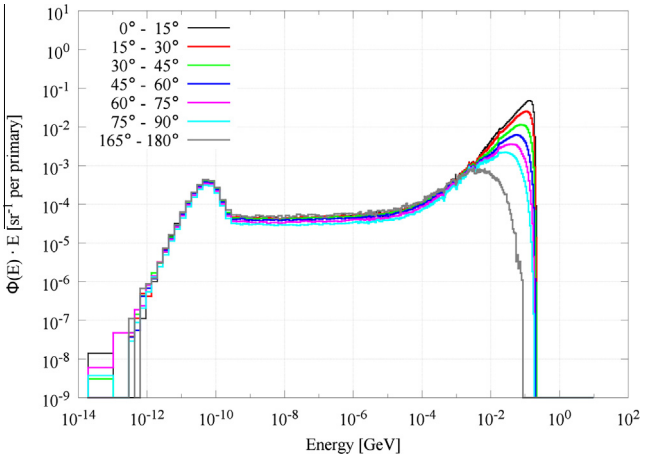

Fig. 3. Neutron energy spectra produced by 215 MeV protons impinging on a tissue target, for some representative angular bins. The spectra in the backward directions (from 90–105° to 165–180°) are rather similar and only the most backward one is shown in the plot.

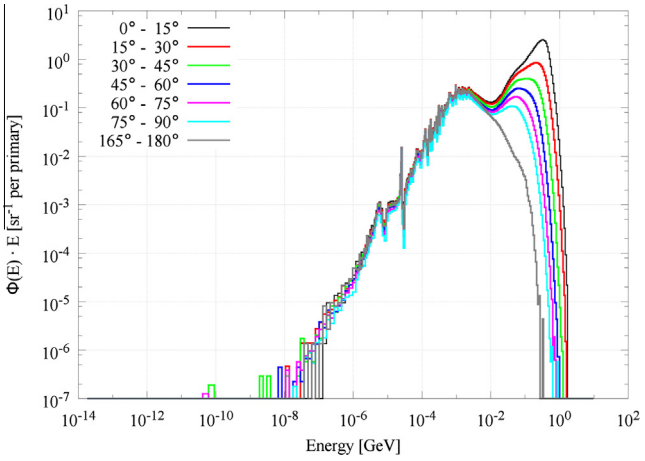

Fig. 4. Neutron energy spectra produced by 469 MeV/amu nitrogen ions impinging on an iron target, for some representative angular bins. The spectra in the backward directions (from 90–105° to 165–180°) are rather similar and only the most backward one is shown in the plot.

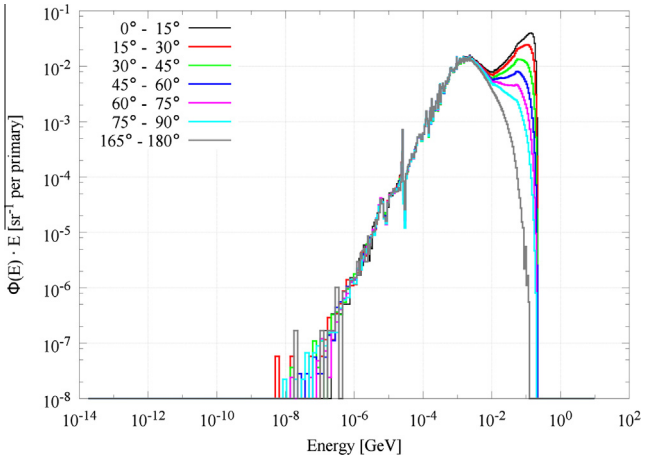

Fig. 2. Neutron energy spectra produced by 215 MeV protons impinging on an iron target, for some representative angular bins. The spectra in the backward directions (from 90–105° to 165–180°) are rather similar and only the most backward one is shown in the plot.

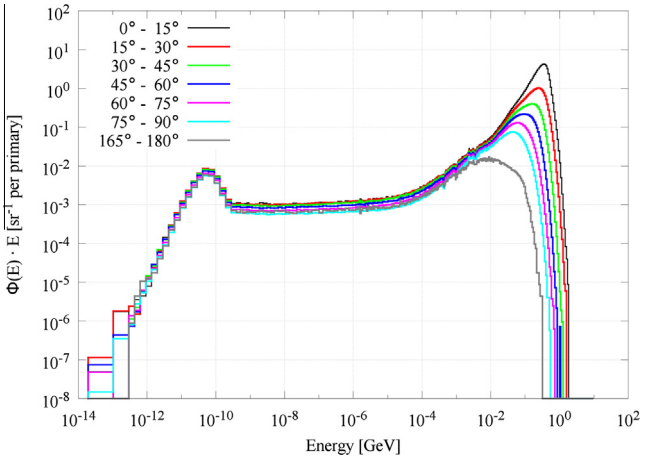

Fig. 5. Neutron energy spectra produced by 469 MeV/amu nitrogen ions impinging on a tissue target, for some representative angular bins. The spectra in the backward directions (from 90–105° to 165–180°) are rather similar and only the most backward one is shown in the plot.

Table 4
Total neutron yield produced by both targets for all incident ion beams.

Ion beam	Energy (MeV/amu)	Total neutron yield (neutrons per primary ion)	
		Iron target	Tissue target
^{1}H	215	0.57 ± 0.01	0.15 ± 0.03
^{4}He	223	2.50 ± 0.01	1.09 ± 0.03
^{7}Li	250	4.55 ± 0.01	2.53 ± 0.02
^{9}Be	286	5.55 ± 0.01	3.12 ± 0.01
^{11}B	342	7.21 ± 0.01	4.07 ± 0.01
^{12}C	430	8.73 ± 0.01	4.71 ± 0.01
^{14}N	469	10.30 ± 0.01	5.55 ± 0.01

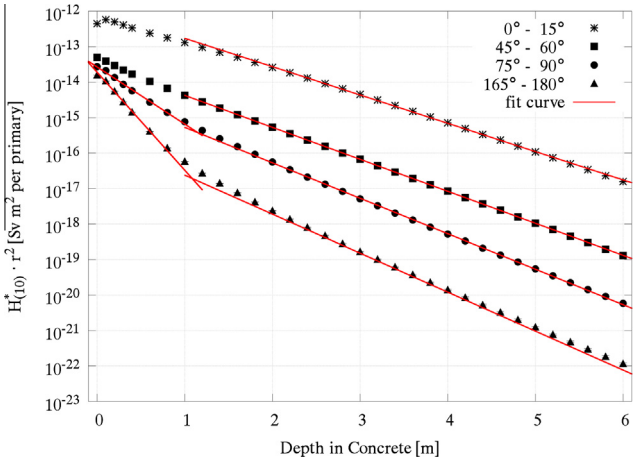

Fig. 6. Attenuation of total dose equivalent in concrete for 496 MeV/amu nitrogen ions impinging on an iron target, for four representative angular bins.

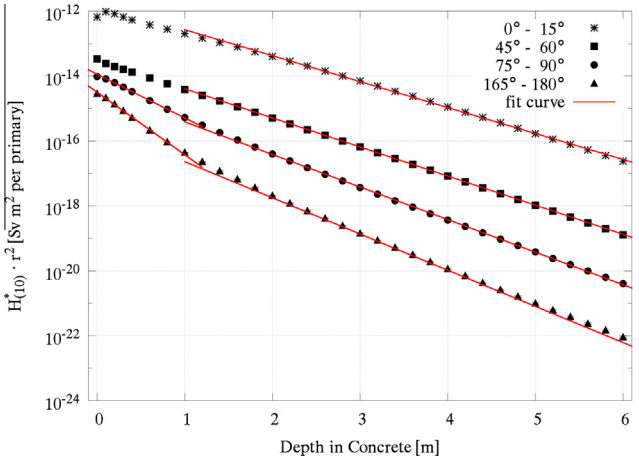

Fig. 7. Attenuation of total dose equivalent in concrete for 496 MeV/amu nitrogen ions impinging on a tissue target, for four representative angular bins.

120–150° for thicknesses up to 4 m, and for the angular bin 150–180° for thicknesses up to 3 m. Results beyond 4 m for the 120–150° bin and beyond 3 m for the 150–180° bin have too high statistical uncertainties and were not included in the fits used for deriving the attenuation curves and the shielding parameters.

The attenuation of the total dose equivalent in a thick shield can be fitted with the classical two-parameter formula [23]:

$$H(E_p, \theta, d/\lambda_\theta) = \frac{H_0(E_p, \theta)}{r^2} \exp\left[-\frac{d}{\lambda_\theta g(a)}\right] \quad (1)$$

where H is the ambient dose equivalent beyond the shield, r the distance between the radiation source (i.e. the target stopping the projectiles) and the point where the dose equivalent is scored, E_p the energy per nucleon of the primary particle, θ the angle between the direction $\vec{r}$ and the beam axis, d the shield thickness, λ_θ the attenuation length for the given shielding material at emission angle θ, H_0 the source term along the direction θ with respect to the beam. The function $g(a) = 1$ is used for the spherical geometry in the present simulations, whereas $g(a) = \cos a$ should be used in all other cases.

Expression (1) was used to fit the data for both shallow penetration (up to 100 cm depth) and deep penetration (after 100 cm depth). It should be mentioned that in the case of shallow penetration, the range of depth values is right after the build-up. Consequently, the neutron spectrum has not yet fully reached equilibrium, leading to an attenuation of the ambient dose equivalent which is not strictly exponential.

At very shallow depths and for forward angles (up to 75°), a dose build-up region is present for all ions. A more or less pronounced dose build-up region is normally present in the first layer of a medium penetrated by radiation, and the type and energy of the secondaries set in motion by the primary radiation affect its intensity profile. In the present case, the build-up is particularly pronounced because it is due to inelastic reactions. The energy distributions harden up to a depth of about 100 cm, after which they reach equilibrium. Moving towards larger angles this situation is reversed and a fast attenuation region appears at small thicknesses, due to the rapid attenuation of the soft component of the spectrum, significantly more populated than the hard one.

The source terms (Sv m^2 per ion) and the attenuation lengths (g cm^{-2}) for all ions and targets, as calculated from the fits to the attenuation curves obtained from the Monte Carlo simulations, are given in Appendix B. Theoretically, H_0 and λ were supposed to be completely geometry independent. However, comparisons made between the secondary neutron yield coming out of the target with and without shielding showed a slight difference due to the effect of the neutron cross-talk, which was not suppressed by the routine used in the simulations (the "cross-talk" represents the neutron transport in one angular bin after being back-scattered from another angular bin, see Refs. [7,8] for a more detailed explanation).

The shielding parameters for each ion differ between the two targets only in the case of shallow penetration, where the attenuation length for the tissue target is longer than for the iron target, most likely because of the much larger number of neutrons with energy below about 1 keV. However, the shielding parameters are quite similar for the two targets in the case of deep penetration because the equilibrium of the neutron spectrum in the shield has been reached.

3.3. Shielding data

The attenuation parameters (source term and attenuation length) are plotted in Figs. 8–15 as a function of angular bin for shallow and deep penetration and for both targets. One sees a clear trend: the higher the energy of the projectile ion, the higher the energy of the neutrons produced and as a consequence the longer the attenuation length. The regularity of these plots is a good indication of the correctness of the fitting procedure that has been applied. However, for deep penetration for the iron target (Fig. 10), in the case of protons and alpha particles there is a deviation from this trend, with the attenuation length of neutrons from protons being slightly longer than the one of neutrons from alpha particles for the angular bins between 60° and 140°. The same inversion is not seen in the case of the tissue target (Fig. 11). This cannot easily be explained, as the spectra for the specific angular bins (Fig. 16

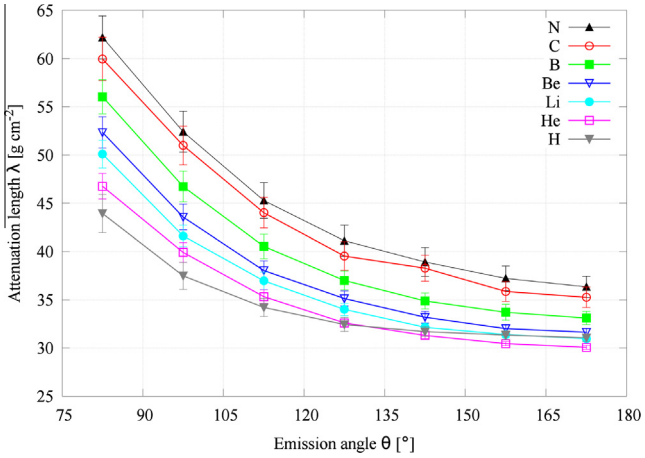

Fig. 8. Attenuation length as a function of scoring angular bin for all ions impinging on an iron target in the case of shallow penetration in a concrete shield.

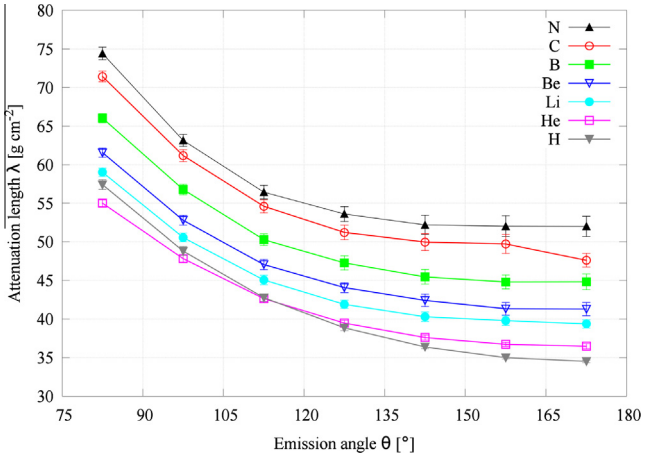

Fig. 9. Attenuation length as a function of scoring angular bin for all ions impinging on a tissue target in the case of shallow penetration in a concrete shield.

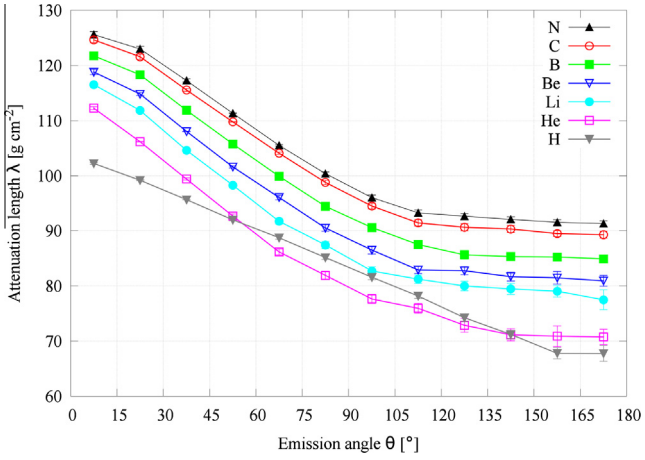

Fig. 10. Attenuation length as a function of scoring angular bin for all ions impinging on an iron target in the case of deep penetration in a concrete shield.

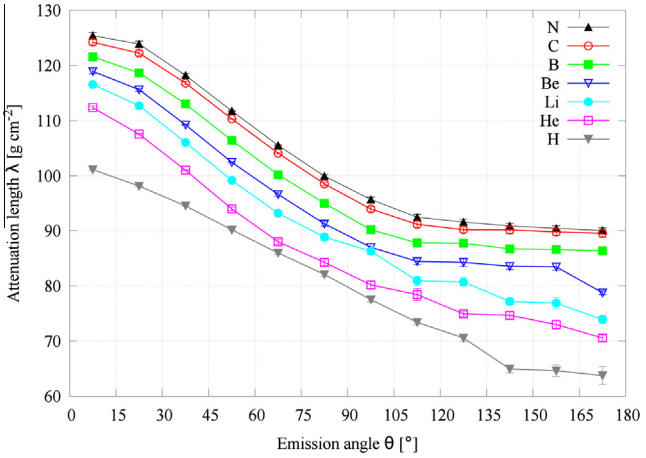

Fig. 11. Attenuation length as a function of scoring angular bin for all ions impinging on a tissue target in the case of deep penetration in a concrete shield.

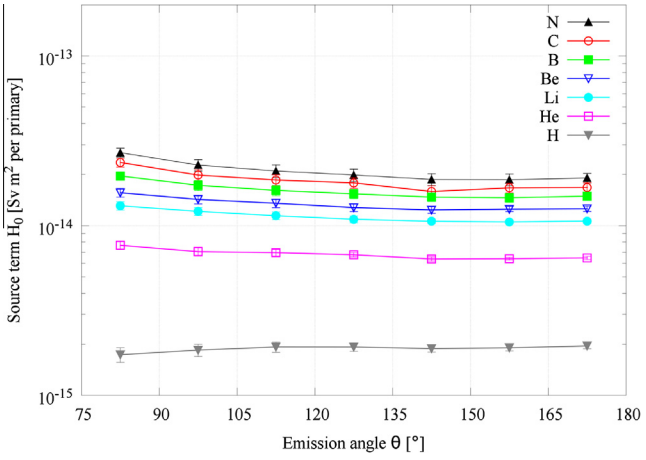

Fig. 12. Source term as a function of scoring angular bin for all ions impinging on an iron target in the case of shallow penetration in a concrete shield.

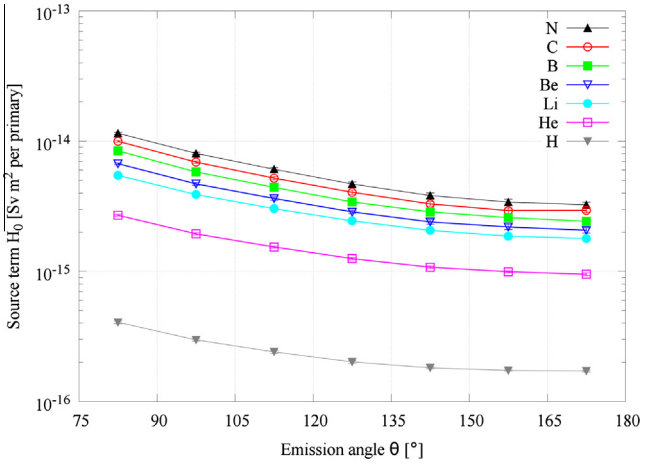

Fig. 13. Source term as a function of scoring angular bin for all ions impinging on a tissue target in the case of shallow penetration in a concrete shield.

and Fig. 17) are similar. It cannot be excluded that in this case the choice of the fitting range (minimum and maximum thickness used to derive the (H_0, λ) parameters) may have some influence on the actual values for some of the angles. Indeed for all ions the fitting procedure for the larger angles is subjected to a somewhat larger uncertainty, due to the reduced fitting range [15].

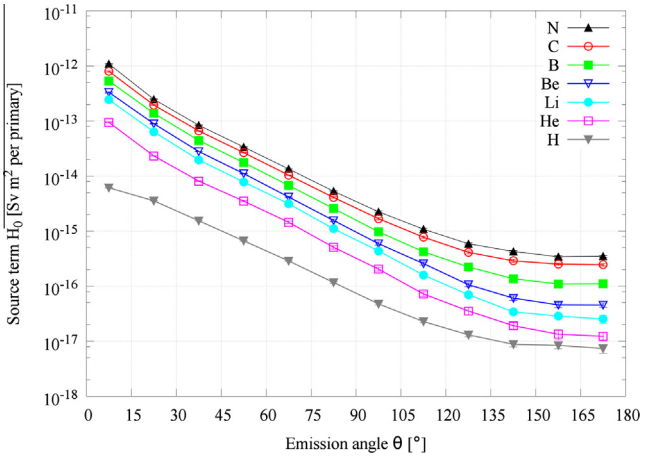

Fig. 14. Source term as a function of scoring angular bin for all ions impinging on an iron target in the case of deep penetration in a concrete shield.

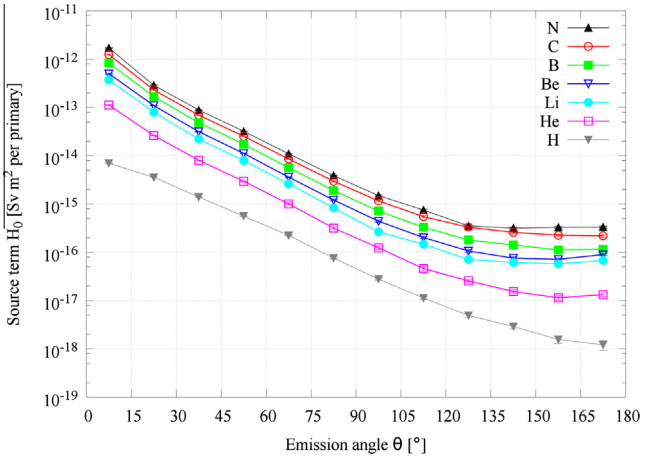

Fig. 15. Source term as a function of scoring angular bin for all ions impinging on a tissue target in the case of deep penetration in a concrete shield.

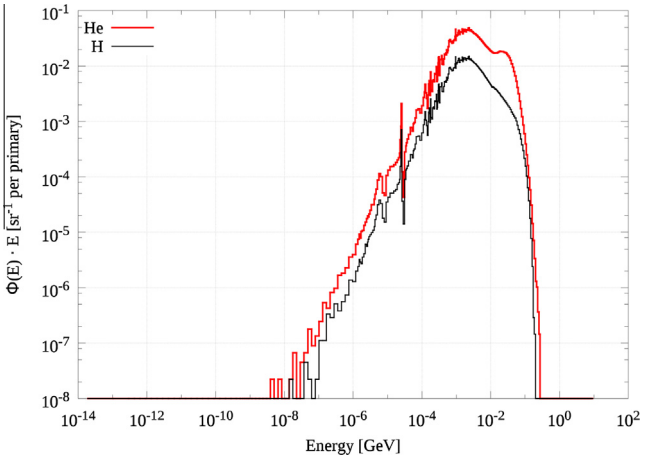

Fig. 16. Neutron energy spectra from protons and alpha particles on an iron target for the angular bin 90–105°.

The variations of the attenuation parameters with the atomic number of the ion Z_{ion} for both shallow and deep penetration are given in Ref. [15]. The attenuation lengths get closer together for

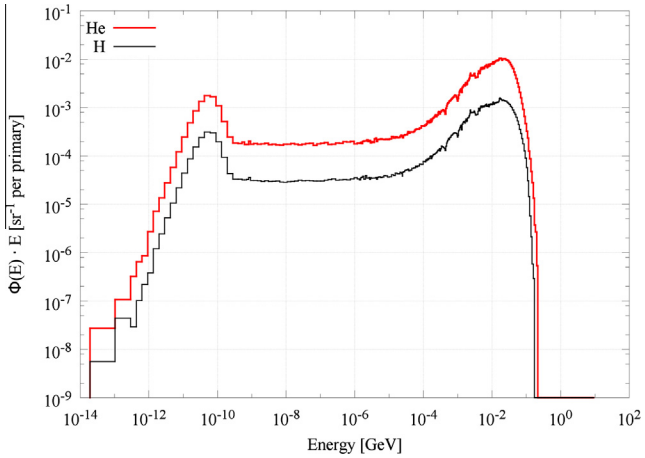

Fig. 17. Neutron energy spectra from protons and alpha particles on a tissue target for the angular bin 90–105°.

emission angles larger than 100°, which is reasonable considering the fact that at backwards angles the soft component of the spectrum, the one less dependent on the ion type, tends to dominate. All curves for both targets show an increase with increasing Z_{ion}, since the energy per nucleon increases with Z_{ion} and so the maximum kinetic energy of the emitted neutrons.

4. Comparison with literature data

Shielding data for ions different than protons are rather scarce in the literature, and always found for specific simulation geometries and experimental set-ups. In this study, the energy for each ion beam was set in order to reach a penetration in ICRU tissue of 290 mm (the typical maximum range required for radiation therapy), the same as that of 430 MeV/amu carbon ions or 215 MeV protons. Some simulations were first performed for 250 MeV protons impinging on an iron target, in order to reproduce the results of a previous study and verify the correctness of the present simulation set-up [7]. These past results [7] were produced with individual simulations for each shielding thickness (and therefore much more time-consuming), as the present routine was not available at that time. The shielding parameters (source terms and attenuation lengths) obtained from the present simulations are consistent with the results of Ref. [7] (Tables 5 and 6). It can be observed that the present work gives, systematically, slightly longer λ-values for deep penetration, and shorter λ-values and larger H_0-values for shallow penetration. It should nonetheless be noted that these discrepancies are reasonable, considering the fact that the fitting process used in the two studies is different. In Ref. [7] the outcome is the average of multiple fitting procedures.

Data are available in the literature for the secondary particle yields from 400 MeV/amu carbon ions and 250 MeV protons incident on thick copper and tissue targets [24], which can be compared with the present results. The comparison was made for three representative angular bins: 0–15°, 45–60°, 75–90°. For each angular bin, the total neutron yield was also calculated (Table 7). All lethargy plots in both linear and logarithmic scale can be found in Ref. [15].

The comparison of the lethargy plots and the total neutron yield show that the present data are consistent with those of Ref. [24]. The per cent difference in the yield varies for the three angular bins and for the different cases, but it mostly stays within 25%, a deviation perfectly acceptable. Deviations in the yields and in the spectra can be explained by the differences between the present study

Table 5
Comparison of source terms and attenuation lengths for shallow penetration in concrete, as calculated in the present study and in Ref. [7].

Shallow penetration				
Angular bin	H_o (10) (Sv m^2 per proton)		λ (g cm^{-2})	
	Ref. [7]	Present study	Ref. [7]	Present study
0–10°	–	–	–	–
40–50°	$(2.3 \pm 0.5)\ 10^{-15}$	$(2.9 \pm 0.2)\ 10^{-15}$	77.0 ± 7.9	69.8 ± 3.5
80–90°	$(1.4 \pm 0.4)\ 10^{-15}$	$(2.0 \pm 0.2)\ 10^{-15}$	49.7 ± 5.7	43.4 ± 2.0
130–140°	$(1.9 \pm 0.6)\ 10^{-15}$	$(2.6 \pm 0.1)\ 10^{-15}$	34.4 ± 3.4	31.5 ± 0.6

Table 6
Comparison of source terms and attenuation lengths for deep penetration in concrete, as calculated in the present study and in Ref. [7].

Deep penetration				
Angular bin	H_o (10) (Sv m^2 per proton)		λ (g cm^{-2})	
	Ref. [7]	Present study	Ref. [7]	Present study
0–10°	$(9.8 \pm 1.0)\ 10^{-15}$	$(9.3 \pm 0.2)\ 10^{-15}$	105.4 ± 1.4	107.9 ± 0.2
40–50°	$(1.2 \pm 0.1)\ 10^{-15}$	$(1.3 \pm 0.1)\ 10^{-15}$	93.5 ± 0.5	97.9 ± 0.1
80–90°	$(9.0 \pm 2.5)\ 10^{-17}$	$(14.1 \pm 0.5)\ 10^{-17}$	83.7 ± 2.0	87.5 ± 0.4
130–140°	$(6.5 \pm 2.6)\ 10^{-18}$	$(1.4 \pm 0.1)\ 10^{-17}$	79.1 ± 3.4	76.6 ± 0.7

Table 7
Neutron yield for three angular bins calculated in the present work and from Ref. [24] for: 250 MeV protons on an iron (present work) or copper target [24], 250 MeV protons on a tissue target, 430 MeV/amu carbon ions on an iron target (present work) and 400 MeV/amu carbon ions on a copper target [24], and 430 MeV/amu (present work) or 400 MeV/amu [24] carbon ions on a tissue target.

	Angular bin	Neutron yield (neutrons per primary ion per steradian)			
		250 MeV p on Fe or 250 MeV p on Cu	250 MeV p on tissue	430 MeV/amu C-ion on Fe or 400 MeV/amu C-ion on Cu	430 MeV/amu C-ion on tissue or 400 MeV/amu C-ion on tissue
Present work	0–15°	1.40 E−01	9.17 E−02	3.87 E+00	4.45 E+00
Ref. [24]	0–10°	1.34 E−01	9.87 E−02	4.23 E+00	5.41 E+00
Present work	45–60°	6.68 E−02	2.25 E−02	0.87 E+00	4.70 E−01
Ref. [24]	40–50°	8.63 E−02	2.82 E−02	1.00 E+00	5.60E−01
Present work	75–90°	4.88 E−02	1.03 E−02	5.37 E−01	1.81 E−01
Ref. [24]	80–90°	7.00 E−02	1.00 E−02	5.31 E−01	1.50 E−01

and Ref. [24]. First, in the two studies the angular bins are not exactly the same but there is a difference of 5° (e.g. 0–15° in the present study versus 0–10° in Ref. [24]), which is probably the main reason for the discrepancies. In the present study, 250 MeV protons impinge on a cylinder of iron 5.8 cm in radius and 7.5 cm thick, in Ref. [24] protons have the same energy but hit a cylinder made of copper, 2.5 cm in radius and 7 cm thick. The main source of the discrepancies in this case is the slight difference in the target thickness, because the thicker is the target, the more are the interactions and the higher is the neutron yield. For the tissue target the discrepancies are negligible.

In the present study, carbon ions of 430 MeV/amu impinge on a right iron cylinder of 6 cm thickness, while in the Ref. [24] carbon ions of 400 MeV/amu impinge on a right copper cylinder of 5 cm thickness. The difference in the beam energy, in the material and dimensions of the target can explain the discrepancies that appear in Table 7. As far as carbon ions on the tissue target are concerned, there are small discrepancies most likely due to the difference in the beam energy and differences in the geometry and dimensions of the target, as the target in Ref. [24] is a slab of 30 cm thickness, whereas in this study it is a right cylinder of 35 cm thickness.

The results of the present study were also compared with the computational data of another study made with various light ions impinging on an ICRU tissue target [25]. A comparison of lethargy plots, in both linear and logarithmic scale, can be found in Ref. [15]. As mentioned above, in the present study the energy of the ion beams was selected in order to provide a range in ICRU tissue of about 29 cm, while the ion energies in Ref. [25] were chosen in order to provide a range in water of about 26.2 cm. The energies of the various ions are compared in Table 8.

Table 8
Energy of the incident ion beams on tissue target as adopted in the present study and in Ref. [25].

Ion beam	Energy (MeV/amu)	
	Present study	Ref. [25]
^{1}H	215	200.0
^{4}He	223	202.0
^{7}Li	250	234.3
^{11}B	342	329.5
^{12}C	430	390.7
^{14}N	469	430.5

The comparison was made for three representative angular bins: 0–15°, 45–60°, 75–90°. For each angular bin, the total neutron yield was calculated (Table 9). The per cent difference in the yield varies for the three bins and for the different ions. The difference in the yield is just a few per cent for lithium ions, it stays below 15–20% for most of the other ions, and it slightly exceeds this value for alpha particles. These discrepancies can be considered more than acceptable and can in general be explained by the differences in the beam energy and profile, and in the target geometry. In Ref. [25] the particle beam is assumed to be circular with 10 mm diameter, and the target is a cylinder 40 cm in thickness and 40 cm in

Table 9
Neutron yield for three angular bins calculated in the present work and from Ref. [25] for various ions impinging on an ICRU tissue target: 215 MeV protons (present work) or 200 MeV protons [25], 223 MeV/amu α particles (present work) or 202 MeV/amu α particles [25], 250 MeV/amu lithium ions (present work) or 234.3 MeV/amu lithium ions [25], 342 MeV/amu boron ions (present work) or 329.5 MeV/amu boron ions [25], 430 MeV/amu carbon ions (present work) or 390.7 MeV/amu carbon ions [25], and 469 MeV/amu nitrogen ions (present work) or 430.5 MeV/amu nitrogen ions [25].

	Angular bin	Neutron yield (neutrons per primary ion per steradian)					
		215 MeV p or 200 MeV p	223 MeV/amu α or 202 MeV/amu α	250 MeV/amu Li or 234.3 MeV/amu Li	342 MeV/amu B or 329.5 MeV/amu B	430 MeV/amu C or 390.7 MeV/amu C	469 MeV/amu N or 430.5 MeV/amu N
Present work	0–15°	7.00 E−02	9.12 E−01	2.53 E+00	4.10 E+00	4.45 E+00	5.41 E+00
Ref. [25]	0–10°	5.37 E−02	7.02 E−01	2.42 E+00	4.77 E+00	4.92 E+00	5.99 E+00
Present work	45–60°	1.56 E−02	10.87 E−02	2.37 E−01	3.91 E−01	4.70 E−01	5.49 E−01
Ref. [25]	40–50°	1.67 E−02	9.35 E−02	2.50 E−01	4.78 E−01	5.69 E−01	6.63 E−01
Present work	75–90°	7.16 E−03	4.66 E−02	9.72 E−02	1.53 E−01	1.81 E−01	2.12 E−01
Ref. [25]	80–90°	7.07 E−03	3.56 E−02	9.03 E−02	1.55 E−01	1.81 E−01	2.09 E−01

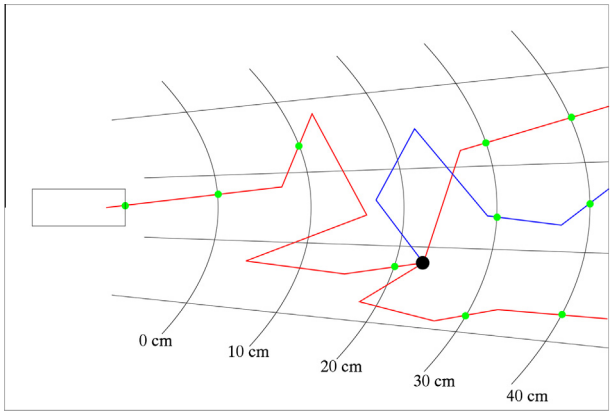

Fig. A.1. How particle tracks and boundary crossing are handled by the user-written FLUKA routine.

diameter. In addition, in the two studies there is a difference of 5° in the angular bins (e.g. 0–15° in the present study versus 0–10° in Ref. [25]), and in the scoring energy range of the neutrons (see Ref. [15]).

There exists a rather extensive compilation of neutron spectra and cross section data from ions [26–28], but very few can be directly compared with the present results. Ref. [27] provides a good compilation of thick target neutron yields and production cross sections for a range of ions. The only data that can be (almost) directly compared with are the total neutron yields for 180 MeV/u ^{4}He and 400 MeV/u ^{12}C ions on a copper target, 0.76 and 3.3 neutrons per ion, respectively. The corresponding figures in the present study are 2.50 and 8.73 neutrons per ion (Table 4). However, the yield data of Ref. [27] are for neutron energy En > 5 MeV and for the 0–90° angular range, whereas data in Table 4 are total neutron yields. Reducing our integration interval to the 0–90° angular range reduces the yield for ^{4}He and ^{12}C to 1.72 and 6.23 neutrons per ion, respectively, and further restricting the yield to En > 5 MeV brings these values down to 1.07 and 4.5 neutrons per ion, respectively. The residual discrepancies with data of Ref. [27] can be explained by the difference in the ion energies, in the target material and dimensions as well as by differences between experimental and computational set-ups. The present data can thus be regarded as in good agreement with those of Ref. [27].

An extensive comparison with literature shielding data (experimental and calculated) for protons was made in a previous study [7]. There are almost no shielding data – source terms and attenuation lengths – for the ions of present and potential therapeutic interest investigated in this paper, except for ^{12}C. The present value of attenuation length for deep penetration in the forward direction for ^{12}C ions on an iron target (Table B.6a) compares very well with data in Ref. [26,27] for 400 MeV/u ^{12}C on a copper target, 126 g cm^{-2} and 115 g cm^{-2} determined experimentally and calculated with the MARS Monte Carlo [29] code, respectively.

5. Conclusions

The present study provides a consistent set of source term and attenuation length data for the shielding design of intermediate energy light ion accelerators. These data should be useful for a first assessment of the shielding requirements of future hadron therapy facilities conceived for operating with ion different than protons or carbon ions. Shielding data have been calculated for the estimated maximum energy of the clinical ion beams.

Table B.1a
Attenuation of total dose equivalent in concrete for 215 MeV protons impinging on an iron target: source terms H_1 and H_2 (Sv m^2 per ion) and attenuation lengths λ_1 and λ_2 (g cm^{-2}) for shallow and deep penetration resulting from the fits to the data.

Protons 215 MeV on iron target				
Angular bin	First exponential		Second exponential	
	H_1 (Sv m^2 per ion)	λ_1 (g cm^{-2})	H_2 (Sv m^2 per ion)	λ_2 (g cm^{-2})
0–15°	–	–	$(6.1 \pm 0.1)\ 10^{-15}$	102.2 ± 0.2
15–30°	–	–	$(35.6 \pm 0.3)\ 10^{-16}$	99.2 ± 0.1
30–45°	–	–	$(154.4 \pm 0.4)\ 10^{-17}$	95.7 ± 0.1
45–60°	–	–	$(66.8 \pm 0.1)\ 10^{-17}$	92.0 ± 0.2
60–75°	–	–	$(28.8 \pm 0.7)\ 10^{-17}$	88.7 ± 0.2
75–90°	$(1.7 \pm 0.2)\ 10^{-15}$	43.9 ± 2.0	$(11.7 \pm 0.4)\ 10^{-17}$	85.2 ± 0.3
90–105°	$(1.8 \pm 0.1)\ 10^{-15}$	37.5 ± 1.4	$(4.8 \pm 0.2)\ 10^{-17}$	81.6 ± 0.4
105–120°	$(1.9 \pm 0.1)\ 10^{-15}$	34.2 ± 0.9	$(2.3 \pm 0.1)\ 10^{-17}$	78.2 ± 0.5
120–135°	$(1.9 \pm 0.1)\ 10^{-15}$	32.4 ± 0.7	$(1.3 \pm 0.1)\ 10^{-17}$	74.2 ± 0.7
135–150°	$(1.9 \pm 0.1)\ 10^{-15}$	31.7 ± 0.5	$(8.9 \pm 0.9)\ 10^{-18}$	71.2 ± 0.8
150–165°	$(1.9 \pm 0.1)\ 10^{-15}$	31.3 ± 0.4	$(8.4 \pm 0.1)\ 10^{-18}$	67.8 ± 1.0
165–180°	$(1.9 \pm 0.1)\ 10^{-15}$	31.1 ± 0.4	$(7.4 \pm 0.1)\ 10^{-18}$	67.8 ± 1.4

Table B.1b
Attenuation of total dose equivalent in concrete for 215 MeV protons impinging on a tissue target: source terms H_1 and H_2 (Sv m^2 per ion) and attenuation lengths λ_1 and λ_2 (g cm^{-2}) for shallow and deep penetration resulting from the fits to the data.

Protons 215 MeV on tissue target				
Angular bin	First exponential		Second exponential	
	H_1 (Sv m^2 per ion)	λ_1 (g cm^2)	H_2 (Sv m^2 per ion)	λ_2 (g cm^{-2})
0–15°	–	–	$(7.0 \pm 0.1)\ 10^{-15}$	101.1 ± 0.1
15–30°	–	–	$(35.9 \pm 0.2)\ 10^{-16}$	98.1 ± 0.1
30–45°	–	–	$(14.0 \pm 0.1)\ 10^{-16}$	94.5 ± 0.1
45–60°	–	–	$(56.2 \pm 0.7)\ 10^{-17}$	90.2 ± 0.1
60–75°	–	–	$(22.5 \pm 0.5)\ 10^{-17}$	86.0 ± 0.2
75–90°	$(4.1 \pm 0.1)\ 10^{-16}$	57.4 ± 0.6	$(7.6 \pm 0.3)\ 10^{-17}$	82.1 ± 0.4
90–105°	$(3.0 \pm 0.1)\ 10^{-16}$	48.8 ± 0.6	$(2.8 \pm 0.1)\ 10^{-17}$	77.5 ± 0.4
105–120°	$(2.4 \pm 0.1)\ 10^{-16}$	42.8 ± 0.5	$(11.3 \pm 0.7)\ 10^{-18}$	73.4 ± 0.5
120–135°	$(2.0 \pm 0.1)\ 10^{-16}$	38.9 ± 0.3	$(4.9 \pm 0.4)\ 10^{-18}$	70.6 ± 0.6
135–150°	$(18.1 \pm 0.3)\ 10^{-17}$	36.4 ± 0.2	$(2.9 \pm 0.3)\ 10^{-18}$	65.0 ± 0.7
150–165°	$(17.3 \pm 0.2)\ 10^{-17}$	35.0 ± 0.2	$(1.6 \pm 0.2)\ 10^{-18}$	64.6 ± 1.0
165–180°	$(17.1 \pm 0.3)\ 10^{-17}$	34.5 ± 0.2	$(1.2 \pm 0.3)\ 10^{-18}$	63.7 ± 1.6

Table B.2a
Attenuation of total dose equivalent in concrete for 223 MeV/amu alpha particles impinging on an iron target: source terms H_1 and H_2 (Sv m^2 per ion) and attenuation lengths λ_1 and λ_2 (g cm^{-2}) for shallow and deep penetration resulting from the fits to the data.

Alphas 223 MeV/amu on iron target				
Angular bin	First exponential		Second exponential	
	H_1 (Sv m^2 per ion)	λ_1 (g cm^{-2})	H_2 (Sv m^2 per ion)	λ_2 (g cm^{-2})
0–15°	–	–	$(94.6 \pm 1.5)\ 10^{-15}$	112.2 ± 0.3
15–30°	–	–	$(23.3 \pm 0.1)\ 10^{-15}$	106.2 ± 0.1
30–45°	–	–	$(8.1 \pm 0.1)\ 10^{-15}$	99.4 ± 0.2
45–60°	–	–	$(3.5 \pm 0.1)\ 10^{-15}$	92.7 ± 0.4
60–75°	–	–	$(1.5 \pm 0.1)\ 10^{-15}$	86.2 ± 0.5
75–90°	$(7.7 \pm 0.4)\ 10^{-15}$	46.7 ± 1.3	$(5.1 \pm 0.4)\ 10^{-16}$	81.9 ± 0.8
90–105°	$(7.0 \pm 0.4)\ 10^{-15}$	39.9 ± 1.0	$(2.0 \pm 0.2)\ 10^{-16}$	77.7 ± 0.9
105–120°	$(6.9 \pm 0.3)\ 10^{-15}$	35.3 ± 0.7	$(7.2 \pm 0.7)\ 10^{-17}$	76.0 ± 0.9
120–135°	$(6.8 \pm 0.2)\ 10^{-15}$	32.6 ± 0.4	$(3.5 \pm 0.5)\ 10^{-17}$	72.9 ± 1.2
135–150°	$(6.3 \pm 0.2)\ 10^{-15}$	31.3 ± 0.3	$(1.9 \pm 0.3)\ 10^{-17}$	71.2 ± 1.1
150–165°	$(6.4 \pm 0.1)\ 10^{-15}$	30.5 ± 0.2	$(1.3 \pm 0.3)\ 10^{-17}$	70.9 ± 1.9
165–180°	$(6.4 \pm 0.1)\ 10^{-15}$	30.1 ± 0.2	$(1.2 \pm 0.2)\ 10^{-17}$	70.8 ± 1.4

Table B.2b
Attenuation of total dose equivalent in concrete for 223 MeV/amu alpha particles impinging on a tissue target: source terms H_1 and H_2 (Sv m^2 per ion) and attenuation lengths λ_1 and λ_2 (g cm^{-2}) for shallow and deep penetration resulting from the fits to the data

Alphas 223 MeV/amu on tissue target				
Angular bin	First exponential		Second exponential	
	H_1 (Sv m^2 per ion)	λ_1 (g cm^{-2})	H_2 (Sv m^2 per ion)	λ_2 (g cm^{-2})
0–15°	–	–	$(11.2 \pm 0.2)\ 10^{-14}$	112.4 ± 0.3
15–30°	–	–	$(26.2 \pm 0.2)\ 10^{-15}$	107.5 ± 0.1
30–45°	–	–	$(8.1 \pm 0.1)\ 10^{-15}$	101.0 ± 0.1
45–60°	–	–	$(3.0 \pm 0.1)\ 10^{-15}$	94.0 ± 0.3
60–75°	–	–	$(10.1 \pm 0.4)\ 10^{-16}$	88.0 ± 0.5
75–90°	$(27.0 \pm 0.4)\ 10^{-16}$	55.0 ± 0.4	$(3.2 \pm 0.2)\ 10^{-16}$	84.3 ± 0.6
90–105°	$(19.4 \pm 0.3)\ 10^{-16}$	47.8 ± 0.5	$(1.2 \pm 0.1)\ 10^{-16}$	80.2 ± 0.7
105–120°	$(15.4 \pm 0.3)\ 10^{-16}$	42.7 ± 0.5	$(4.6 \pm 0.5)\ 10^{-17}$	78.4 ± 1.1
120–135°	$(12.5 \pm 0.3)\ 10^{-16}$	39.5 ± 0.4	$(2.6 \pm 0.1)\ 10^{-17}$	75.0 ± 0.5
135–150°	$(10.8 \pm 0.2)\ 10^{-16}$	37.6 ± 0.3	$(1.6 \pm 0.1)\ 10^{-17}$	74.7 ± 0.6
150–165°	$(10.2 \pm 0.2)\ 10^{-16}$	36.7 ± 0.2	$(1.1 \pm 0.1)\ 10^{-17}$	73.0 ± 0.8
165–180°	$(9.5 \pm 0.2)\ 10^{-16}$	36.5 ± 0.3	$(1.3 \pm 0.1)\ 10^{-17}$	70.6 ± 0.6

The attenuation parameters – source terms and attenuation lengths – are given as a function of angular bin for shallow and deep penetration. The attenuation curves follow a clear trend, according to which the higher the energy of the projectile ion, the more penetrating is the neutron spectrum and the longer is the attenuation length of neutrons in the shielding material (concrete in the present study). The dependence of the attenuation parameters upon the atomic number of the ion, Z_{ion}, for both shallow and deep penetration [15] show that the attenuation lengths tend to get closer as Z_{ion} increases due to the fact that the available energy increases. However, from a certain point saturation begins for both targets. The regularity of these plots is a strong indication of the fact that the fitting procedure that has been applied is correct.

Table B.3a
Attenuation of total dose equivalent in concrete for 250 MeV/amu lithium ions impinging on an iron target: source terms H_1 and H_1 (Sv m^2 per ion) and attenuation lengths λ_1 and λ_2 (g cm^{-2}) for shallow and deep penetration resulting from the fits to the data.

Lithium 250 MeV/amu on iron target				
Angular Bin	First exponential		Second exponential	
	H_1 (Sv m^2 per ion)	λ_1 (g cm^{-2})	H_2 (Sv m^2 per ion)	λ_2 (g cm^{-2})
0–15°	–	–	$(24.4 \pm 0.5)\ 10^{-14}$	116.5 ± 0.4
15–30°	–	–	$(63.8 \pm 0.7)\ 10^{-15}$	111.8 ± 0.2
30–45°	–	–	$(19.7 \pm 0.1)\ 10^{-15}$	104.6 ± 0.1
45–60°	–	–	$(7.8 \pm 0.2)\ 10^{-15}$	98.3 ± 0.3
60–75°	–	–	$(3.1 \pm 0.1)\ 10^{-15}$	91.7 ± 0.5
75–90°	$(13.1 \pm 0.7)\ 10^{-15}$	50.1 ± 1.4	$(1.1 \pm 0.1)\ 10^{-15}$	87.5 ± 0.7
90–105°	$(12.1 \pm 0.6)\ 10^{-15}$	41.6 ± 1.1	$(4.4 \pm 0.3)\ 10^{-16}$	82.7 ± 0.7
105–120°	$(11.4 \pm 0.6)\ 10^{-15}$	37.0 ± 0.9	$(1.6 \pm 0.1)\ 10^{-16}$	81.3 ± 0.7
120–135°	$(10.9 \pm 0.5)\ 10^{-15}$	34.0 ± 0.6	$(0.7 \pm 0.1)\ 10^{-16}$	80.0 ± 0.8
135–150°	$(10.6 \pm 0.3)\ 10^{-15}$	32.1 ± 0.4	$(3.4 \pm 0.4)\ 10^{-17}$	79.5 ± 1.0
150–165°	$(10.5 \pm 0.3)\ 10^{-15}$	31.4 ± 0.3	$(2.9 \pm 0.3)\ 10^{-17}$	79.1 ± 1.0
165–180°	$(10.6 \pm 0.3)\ 10^{-15}$	31.0 ± 0.3	$(2.5 \pm 0.4)\ 10^{-17}$	77.5 ± 1.8

Table B.3b
Attenuation of total dose equivalent in concrete for 250 MeV/amu lithium ions impinging on a tissue target: source terms H_1 and H_2 (Sv m^2 per ion) and attenuation lengths λ_1 and λ_2 (g cm^{-2}) for shallow and deep penetration resulting from the fits to the data.

Lithium 250 MeV/amu on tissue target				
Angular bin	First exponential		Second exponential	
	H_1 (Sv m^2 per ion)	λ_1 (g cm^{-2})	H_2 (Sv m^2 per ion)	λ_2 (g cm^{-2})
0–15°	–	–	$(37.4 \pm 0.8)\ 10^{-14}$	116.6 ± 0.4
15–30°	–	–	$(8.0 \pm 0.1)\ 10^{-14}$	112.7 ± 0.2
30–45°	–	–	$(2.2 \pm 0.5)\ 10^{-14}$	106.0 ± 0.1
45–60°	–	–	$(8.0 \pm 0.1)\ 10^{-15}$	99.2 ± 0.2
60–75°	–	–	$(2.6 \pm 0.1)\ 10^{-15}$	93.2 ± 0.4
75–90°	$(54.6 \pm 0.8)\ 10^{-16}$	59.0 ± 0.5	$(8.3 \pm 0.5)\ 10^{-16}$	88.9 ± 0.6
90–105°	$(38.9 \pm 0.9)\ 10^{-16}$	50.6 ± 0.6	$(2.7 \pm 0.2)\ 10^{-16}$	86.3 ± 0.6
105–120°	$(30.3 \pm 0.8)\ 10^{-16}$	45.1 ± 0.6	$(1.5 \pm 0.1)\ 10^{-16}$	81.0 ± 0.8
120–135°	$(24.4 \pm 0.6)\ 10^{-16}$	41.9 ± 0.5	$(7.1 \pm 0.6)\ 10^{-17}$	80.7 ± 0.8
135–150°	$(20.6 \pm 0.7)\ 10^{-16}$	40.3 ± 0.6	$(6.2 \pm 0.4)\ 10^{-17}$	77.2 ± 0.6
150–165°	$(18.6 \pm 0.6)\ 10^{-16}$	39.8 ± 0.6	$(5.8 \pm 0.6)\ 10^{-17}$	76.9 ± 1.0
165–180°	$(17.9 \pm 0.6)\ 10^{-16}$	39.4 ± 0.5	$(6.8 \pm 0.5)\ 10^{-17}$	73.9 ± 0.7

Table B.4a
Attenuation of total dose equivalent in concrete for 286 MeV/amu beryllium ions impinging on an iron target: source terms H_1 and H_2 (Sv m^2 per ion) and attenuation lengths λ_1 and λ_2 (g cm^{-2}) for shallow and deep penetration resulting from the fits to the data.

Beryllium 286 MeV/amu on iron target				
Angular Bin	First exponential		Second exponential	
	H_1 (Sv m^2 per ion)	λ_1 (g cm^{-2})	H_2 (Sv m^2 per ion)	λ_2 (g cm^{-2})
0–15°	–	–	$(33.1 \pm 0.8)\ 10^{-14}$	118.8 ± 0.4
15–30°	–	–	$(89.5 \pm 1.3)\ 10^{-15}$	114.8 ± 0.2
30–45°	–	–	$(28.0 \pm 0.1)\ 10^{-15}$	108.0 ± 0.1
45–60°	–	–	$(11.1 \pm 0.2)\ 10^{-15}$	101.6 ± 0.2
60–75°	–	–	$(4.2 \pm 0.1)\ 10^{-15}$	96.0 ± 0.4
75–90°	$(15.6 \pm 0.9)\ 10^{-15}$	52.3 ± 1.6	$(1.6 \pm 0.1)\ 10^{-15}$	90.5 ± 0.6
90–105°	$(14.3 \pm 0.8)\ 10^{-15}$	43.6 ± 1.3	$(5.9 \pm 0.4)\ 10^{-16}$	86.5 ± 0.7
105–120°	$(13.5 \pm 0.8)\ 10^{-15}$	38.0 ± 1.0	$(2.6 \pm 0.2)\ 10^{-16}$	82.9 ± 0.7
120–135°	$(12.8 \pm 0.7)\ 10^{-15}$	35.1 ± 0.8	$(1.1 \pm 0.1)\ 10^{-16}$	82.8 ± 0.7
135–150°	$(12.4 \pm 0.5)\ 10^{-15}$	33.2 ± 0.6	$(6.1 \pm 0.5)\ 10^{-17}$	81.7 ± 0.8
150–165°	$(12.5 \pm 0.4)\ 10^{-15}$	32.0 ± 0.4	$(4.6 \pm 0.5)\ 10^{-17}$	81.5 ± 1.1
165–180°	$(12.6 \pm 0.4)\ 10^{-15}$	31.6 ± 0.4	$(4.5 \pm 0.4)\ 10^{-17}$	80.9 ± 1.0

A comparison with the few computational data available in the literature [24–27] of the spectra of the secondary neutrons generated from both targets for different incident ion beams and of the secondary neutron yields, shows that discrepancies can be understood and the agreement can be regarded as satisfactory.

Acknowledgements

The authors wish to thank M. Ferrarini (CNAO, Pavia, Italy) and A. Porta (Polytechnic of Milan), for providing the numerical data of Refs. [24] and [25].

Table B.4b
Attenuation of total dose equivalent in concrete for 286 MeV/amu beryllium ions impinging on a tissue target: source terms H_1 and H_2 (Sv m^2 per ion) and attenuation lengths λ_1 and λ_2 (g cm^{-2}) for shallow and deep penetration resulting from the fits to the data.

Beryllium 286 MeV/amu on tissue target				
Angular Bin	First exponential		Second exponential	
	H_1 (Sv m^2 per ion)	λ_1 (g cm^{-2})	H_2 (Sv m^2 per ion)	λ_2 (g cm^{-2})
0–15°	–	–	$(50.1 \pm 1.2)\ 10^{-14}$	118.9 ± 0.4
15–30°	–	–	$(109.5 \pm 1.9)\ 10^{-15}$	115.6 ± 0.3
30–45°	–	–	$(31.5 \pm 0.2)\ 10^{-15}$	109.2 ± 0.1
45–60°	–	–	$(112.1 \pm 0.8)\ 10^{-16}$	102.4 ± 0.1
60–75°	–	–	$(36.1 \pm 0.9)\ 10^{-16}$	96.6 ± 0.3
75–90°	$(6.7 \pm 0.1)\ 10^{-15}$	61.6 ± 0.6	$(12.1 \pm 0.4)\ 10^{-16}$	91.3 ± 0.4
90–105°	$(4.7 \pm 0.1)\ 10^{-15}$	52.8 ± 0.6	$(4.4 \pm 0.2)\ 10^{-16}$	87.0 ± 0.6
105–120°	$(3.6 \pm 0.1)\ 10^{-15}$	47.1 ± 0.7	$(2.0 \pm 0.1)\ 10^{-16}$	84.5 ± 0.6
120–135°	$(28.6 \pm 0.9)\ 10^{-16}$	44.1 ± 0.6	$(1.2 \pm 0.1)\ 10^{-16}$	84.3 ± 0.8
135–150°	$(24.0 \pm 0.9)\ 10^{-16}$	42.4 ± 0.8	$(7.6 \pm 0.5)\ 10^{-17}$	83.6 ± 0.6
150–165°	$(21.9 \pm 1.0)\ 10^{-16}$	41.4 ± 0.8	$(7.2 \pm 0.4)\ 10^{-17}$	83.5 ± 0.6
165–180°	$(20.7 \pm 1.0)\ 10^{-16}$	41.3 ± 0.8	$(9.0 \pm 0.4)\ 10^{-17}$	78.8 ± 0.4

Table B.5a
Attenuation of total dose equivalent in concrete for 342 MeV/amu boron ions impinging on an iron target: source terms H_1 and H_2 (Sv m^2 per ion) and attenuation lengths λ_1 and λ_2 (g cm^{-2}) for shallow and deep penetration resulting from the fits to the data.

Boron 342 MeV/amu on iron target				
Angular bin	First exponential		Second exponential	
	H_1 (Sv m^2 per ion)	λ_1 (g cm^{-2})	H_2 (Sv m^2 per ion)	λ_2 (g cm^{-2})
0–15°	–	–	$(53.6 \pm 1.3)\ 10^{-14}$	121.8 ± 0.5
15–30°	–	–	$(13.8 \pm 0.3)\ 10^{-14}$	118.3 ± 0.3
30–45°	–	–	$(44.5 \pm 0.3)\ 10^{-15}$	111.9 ± 0.1
45–60°	–	–	$(17.6 \pm 0.1)\ 10^{-15}$	105.8 ± 0.1
60–75°	–	–	$(6.8 \pm 0.1)\ 10^{-15}$	99.9 ± 0.3
75–90°	$(19.6 \pm 1.1)\ 10^{-15}$	56.0 ± 1.8	$(2.6 \pm 0.1)\ 10^{-15}$	94.4 ± 0.5
90–105°	$(17.3 \pm 1.2)\ 10^{-15}$	46.7 ± 1.6	$(9.7 \pm 0.5)\ 10^{-16}$	90.6 ± 0.6
105–120°	$(16.1 \pm 1.1)\ 10^{-15}$	40.5 ± 1.3	$(4.2 \pm 0.2)\ 10^{-16}$	87.5 ± 0.6
120–135°	$(15.4 \pm 0.9)\ 10^{-15}$	37.0 ± 1.0	$(2.2 \pm 0.2)\ 10^{-16}$	85.7 ± 0.8
135–150°	$(14.7 \pm 0.9)\ 10^{-15}$	34.9 ± 0.8	$(1.4 \pm 0.1)\ 10^{-16}$	85.3 ± 0.7
150–165°	$(14.6 \pm 0.9)\ 10^{-15}$	33.7 ± 0.8	$(11.0 \pm 0.5)\ 10^{-17}$	85.3 ± 0.5
165–180°	$(14.9 \pm 0.7)\ 10^{-15}$	33.1 ± 0.7	$(11.1 \pm 0.6)\ 10^{-17}$	84.9 ± 0.6

Table B.5b
Attenuation of total dose equivalent in concrete for 342 MeV/amu boron ions impinging on a tissue target: source terms H_1 and H_2 (Sv m^2 per ion) and attenuation lengths λ_1 and λ_2 (g cm^{-2}) for shallow and deep penetration resulting from the fits to the data.

Boron 342 MeV/amu on tissue target				
Angular bin	First exponential		Second exponential	
	H_1 (Sv m^2 per ion)	λ_1 (g cm^{-2})	H_2 (Sv m^2 per ion)	λ_2 (g cm^{-2})
0–15°	–	–	$(84.0 \pm 2.2)\ 10^{-14}$	121.6 ± 0.5
15–30°	–	–	$(16.8 \pm 0.4)\ 10^{-14}$	118.7 ± 0.4
30–45°	–	–	$(48.7 \pm 0.5)\ 10^{-15}$	113.0 ± 0.2
45–60°	–	–	$(17.4 \pm 0.1)\ 10^{-15}$	106.4 ± 0.1
60–75°	–	–	$(5.7 \pm 0.1)\ 10^{-15}$	100.2 ± 0.2
75–90°	$(84.4 \pm 1.2)\ 10^{-16}$	66.0 ± 0.6	$(1.9 \pm 0.1)\ 10^{-15}$	95.0 ± 0.4
90–105°	$(58.0 \pm 1.4)\ 10^{-16}$	56.8 ± 0.7	$(7.2 \pm 0.4)\ 10^{-16}$	90.2 ± 0.6
105–120°	$(44.2 \pm 1.4)\ 10^{-16}$	50.3 ± 0.8	$(3.3 \pm 0.2)\ 10^{-16}$	87.8 ± 0.6
120–135°	$(34.1 \pm 1.6)\ 10^{-16}$	47.3 ± 0.9	$(1.8 \pm 0.1)\ 10^{-16}$	87.8 ± 0.6
135–150°	$(28.6 \pm 1.2)\ 10^{-16}$	45.5 ± 0.9	$(1.4 \pm 0.1)\ 10^{-16}$	86.8 ± 0.6
150–165°	$(25.9 \pm 1.0)\ 10^{-16}$	44.8 ± 0.9	$(1.1 \pm 0.1)\ 10^{-16}$	86.6 ± 0.6
165–180°	$(24.2 \pm 1.2)\ 10^{-16}$	44.8 ± 1.0	$(1.2 \pm 0.1)\ 10^{-16}$	86.4 ± 0.6

Appendix A. FLUKA routine implemented for boundary crossing scoring

The ambient dose equivalent outside a shield of a given thickness is properly estimated at the boundary between the shield and the surrounding vacuum or air. Such a method requires a dedicated simulation for every thickness of interest, with the consequent need of huge CPU times. The use of boundary crossing estimators at different depths inside the shield drastically reduces the required CPU time, but results are overestimated because of particles scattered back and forth across any given estimator. Results would be impacted especially when the contribution from neutrons slowing down is non-negligible, and in case of materials with significant fractions of light elements, in particular hydrogen.

Table B.6a
Attenuation of total dose equivalent in concrete for 430 MeV/amu carbon ions impinging on an iron target: source terms H_1 and H_2 (Sv m^2 per ion) and attenuation lengths λ_1 and λ_2 (g cm^{-2}) for shallow and deep penetration resulting from the fits to the data.

Carbon 430 MeV/amu on iron target				
Angular bin	First exponential		Second exponential	
	H_1 (Sv m^2 per ion)	λ_1 (g cm^{-2})	H_2 (Sv m^2 per ion)	λ_2 (g cm^{-2})
0–15°	–	–	$(80.0 \pm 2.1)\ 10^{-14}$	124.7 ± 0.5
15–30°	–	–	$(19.5 \pm 0.4)\ 10^{-14}$	121.6 ± 0.4
30–45°	–	–	$(66.3 \pm 0.9)\ 10^{-15}$	115.6 ± 0.2
45–60°	–	–	$(26.6 \pm 0.1)\ 10^{-15}$	109.8 ± 0.1
60–75°	–	–	$(10.4 \pm 0.1)\ 10^{-15}$	104.1 ± 0.2
75–90°	$(23.6 \pm 1.4)\ 10^{-15}$	60.0 ± 2.2	$(4.1 \pm 0.1)\ 10^{-15}$	98.8 ± 0.4
90–105°	$(19.9 \pm 1.5)\ 10^{-15}$	51.0 ± 2.0	$(1.7 \pm 0.1)\ 10^{-15}$	94.5 ± 0.5
105–120°	$(18.6 \pm 1.4)\ 10^{-15}$	44.0 ± 1.6	$(7.8 \pm 0.4)\ 10^{-16}$	91.4 ± 0.6
120–135°	$(17.9 \pm 1.3)\ 10^{-15}$	39.5 ± 1.5	$(4.1 \pm 0.2)\ 10^{-16}$	90.6 ± 0.6
135–150°	$(15.9 \pm 1.3)\ 10^{-15}$	38.3 ± 1.3	$(2.9 \pm 0.2)\ 10^{-17}$	90.3 ± 0.6
150–165°	$(16.7 \pm 1.1)\ 10^{-15}$	35.9 ± 1.0	$(2.5 \pm 0.1)\ 10^{-17}$	89.5 ± 0.5
165–180°	$(16.8 \pm 1.1)\ 10^{-15}$	35.3 ± 1.1	$(2.5 \pm 0.1)\ 10^{-17}$	89.3 ± 0.6

Table B.6b
Attenuation of total dose equivalent in concrete for 430 MeV/amu carbon ions impinging on a tissue target: source terms H_1 and H_2 (Sv m^2 per ion) and attenuation lengths λ_1 and λ_2 (g cm^{-2}) for shallow and deep penetration resulting from the fits to the data.

Carbon 430 MeV/amu on tissue target				
Angular bin	First exponential		Second exponential	
	H_1 (Sv m^2 per ion)	λ_1 (g cm^{-2})	H_2 (Sv m^2 per ion)	λ_2 (g cm^{-2})
0–15°	–	–	$(124.5 \pm 3.4)\ 10^{-14}$	124.2 ± 0.5
15–30°	–	–	$(231.4 \pm 6.0)\ 10^{-15}$	122.2 ± 0.5
30–45°	–	–	$(69.6 \pm 1.1)\ 10^{-15}$	116.8 ± 0.3
45–60°	–	–	$(25.3 \pm 0.1)\ 10^{-15}$	110.3 ± 0.1
60–75°	–	–	$(8.6 \pm 0.1)\ 10^{-15}$	104.1 ± 0.1
75–90°	$(10.0 \pm 0.1)\ 10^{-15}$	71.4 ± 0.7	$(3.0 \pm 0.1)\ 10^{-15}$	98.5 ± 0.3
90–105°	$(6.9 \pm 0.2)\ 10^{-15}$	61.2 ± 0.8	$(11.6 \pm 0.4)\ 10^{-16}$	93.9 ± 0.4
105–120°	$(5.2 \pm 0.1)\ 10^{-15}$	54.6 ± 0.9	$(5.5 \pm 0.3)\ 10^{-16}$	91.2 ± 0.6
120–135°	$(4.0 \pm 0.1)\ 10^{-15}$	51.2 ± 0.9	$(3.3 \pm 0.1)\ 10^{-16}$	90.2 ± 0.5
135–150°	$(3.3 \pm 0.1)\ 10^{-15}$	50.0 ± 1.1	$(2.6 \pm 0.1)\ 10^{-16}$	90.2 ± 0.7
150–165°	$(2.9 \pm 0.1)\ 10^{-15}$	49.7 ± 1.2	$(2.3 \pm 0.1)\ 10^{-16}$	89.8 ± 0.6
165–180°	$(2.9 \pm 0.1)\ 10^{-15}$	47.6 ± 0.9	$(2.2 \pm 0.1)\ 10^{-16}$	89.5 ± 0.7

Table B.7a
Attenuation of total dose equivalent in concrete for 469 MeV/amu nitrogen ions impinging on an iron target: source terms H_1 and H_2 (Sv m^2 per ion) and attenuation lengths λ_1 and λ_2 (g cm^{-2}) for shallow and deep penetration resulting from the fits to the data.

Nitrogen 469 MeV/amu on iron target				
Angular bin	First exponential		Second exponential	
	H_1 (Sv m^2 per ion)	λ_1 (g cm^{-2})	H_2 (Sv m^2 per ion)	λ_2 (g cm^{-2})
0–15°	–	–	$(10.9 \pm 0.3)\ 10^{-13}$	125.6 ± 0.5
15–30°	–	–	$(2.5 \pm 0.1)\ 10^{-13}$	123.0 ± 0.5
30–45°	–	–	$(83.8 \pm 1.3)\ 10^{-15}$	117.3 ± 0.3
45–60°	–	–	$(33.8 \pm 0.1)\ 10^{-15}$	111.3 ± 0.1
60–75°	–	–	$(13.5 \pm 0.1)\ 10^{-15}$	105.5 ± 0.1
75–90°	$(26.9 \pm 1.7)\ 10^{-15}$	62.2 ± 2.2	$(5.3 \pm 0.1)\ 10^{-15}$	100.4 ± 0.3
90–105°	$(22.8 \pm 1.8)\ 10^{-15}$	52.4 ± 2.1	$(22.5 \pm 0.8)\ 10^{-16}$	96.0 ± 0.4
105–120°	$(21.0 \pm 1.8)\ 10^{-15}$	45.3 ± 1.8	$(10.9 \pm 0.5)\ 10^{-16}$	93.3 ± 0.5
120–135°	$(19.9 \pm 1.6)\ 10^{-15}$	41.1 ± 1.6	$(5.9 \pm 0.3)\ 10^{-16}$	92.7 ± 0.5
135–150°	$(18.7 \pm 1.5)\ 10^{-15}$	38.9 ± 1.5	$(4.3 \pm 0.2)\ 10^{-16}$	92.1 ± 0.5
150–165°	$(18.7 \pm 1.5)\ 10^{-15}$	37.2 ± 1.3	$(3.6 \pm 0.1)\ 10^{-16}$	91.8 ± 0.5
165–180°	$(19.1 \pm 1.3)\ 10^{-15}$	36.3 ± 1.1	$(3.5 \pm 0.1)\ 10^{-16}$	91.3 ± 0.5

Thus, the attenuation curves featuring relatively soft neutron spectra may be affected by this effect, especially those obtained at the largest emission angles, and in case of the lightest ions [7,8].

In order to overcome this issue, the scoring of a given particle must be triggered at a given boundary crossing estimator only if the particle is seen for the first time at the current depth in the shield, no matter the angular bin. This condition is satisfied when the maximum depth reached by the particle is lower than the depth at which the scoring is performed. Every particle is thus assigned a variable which stores the maximum scoring depth

Table B.7b
Attenuation of total dose equivalent in concrete for 469 MeV/amu nitrogen ions impinging on a tissue target: source terms H_1 and H_2 (Sv m^2 per ion) and attenuation lengths λ_1 and λ_2 (g cm^{-2}) for shallow and deep penetration resulting from the fits to the data.

Nitrogen 469 MeV/amu on tissue target				
Angular bin	First exponential		Second exponential	
	H_1 (Sv m^2 per ion)	λ_1 (g cm^{-2})	H_2 (Sv m^2 per ion)	λ_2 (g cm^{-2})
0–15°	–	–	$(17.0 \pm 0.5)\ 10^{-13}$	125.4 ± 0.5
15–30°	–	–	$(28.9 \pm 0.8)\ 10^{-14}$	123.9 ± 0.5
30–45°	–	–	$(8.9 \pm 0.2)\ 10^{-14}$	118.2 ± 0.3
45–60°	–	–	$(32.2 \pm 0.2)\ 10^{-15}$	111.8 ± 0.1
60–75°	–	–	$(11.0 \pm 0.1)\ 10^{-15}$	105.5 ± 0.1
75–90°	$(11.5 \pm 0.2)\ 10^{-15}$	74.4 ± 0.8	$(3.9 \pm 0.1)\ 10^{-15}$	99.9 ± 0.3
90–105°	$(8.1 \pm 0.2)\ 10^{-15}$	63.1 ± 0.8	$(1.5 \pm 0.1)\ 10^{-15}$	95.7 ± 0.4
105–120°	$(6.1 \pm 0.2)\ 10^{-15}$	56.4 ± 0.9	$(7.5 \pm 0.3)\ 10^{-16}$	92.5 ± 0.5
120–135°	$(4.7 \pm 0.2)\ 10^{-15}$	53.6 ± 1.0	$(3.5 \pm 0.2)\ 10^{-16}$	91.6 ± 0.5
135–150°	$(3.8 \pm 0.2)\ 10^{-15}$	52.2 ± 1.2	$(3.2 \pm 0.1)\ 10^{-16}$	90.9 ± 0.5
150–165°	$(3.4 \pm 0.2)\ 10^{-15}$	52.0 ± 1.3	$(3.3 \pm 0.1)\ 10^{-16}$	90.4 ± 0.5
165–180°	$(3.2 \pm 0.2)\ 10^{-15}$	52.0 ± 1.3	$(3.3 \pm 0.1)\ 10^{-16}$	90.0 ± 0.5

reached, while each boundary crossing estimator is assigned the depth at which it is performed, no matter its actual angular bin. Whenever a particle is seen by a boundary crossing estimator, the depth of which is greater than the value stored for the particle, the particle is scored, and the associated value of maximum depth updated accordingly. Particles generated in the target get their associated value of maximum depth when they actually leave the target; particle generated in the shield inherit the value associated to the parent particle.

The red path in Fig. A.1 shows an example of a possible particle track, and the small green dots mark the only boundary crossings that should be scored. The variable storing the maximum depth in the shield reached by the particle is initialised to a fictitious negative value when the particle exits from the target: once at the shielding surface (at 0 cm depth), the scoring is performed, and the maximum depth reached by the particle is updated to 0. At the following step, at the crossing of the boundary at 10 cm, the same happens again: since the maximum depth previously reached by the particle is 0 cm, the scoring is performed, and the variable storing the maximum depth reached by the particle is updated to 10 cm. When the same particle crosses again the same boundary going outwards, the scoring is not performed, since the particle had already reached that depth and was already scored. The large black dot some steps afterwards represents an inelastic event, in which the parent particle dies and three new particles are created, inheriting the maximum depth reached by the parent particle for proper scoring (see for instance the light blue path). It should be noted that the tracked particle is scored also in angular bins different from the original one.

The value of maximum depth associated to each particle is stored in one of the spare variables available to the user, so that new particles automatically inherit the value of the parent one. Each boundary crossing estimator is labelled with its depth. A user-written routine, linked to FLUKA, checks the depth and in case triggers the scoring and updates the value associated to the current particle.

Appendix B. Attenuation parameters

Tables B.1–B.7 provide source terms H_o (Sv m^2 per ion) and attenuation lengths λ (g cm^{-2}) for all ions and targets, calculated from the fits to the attenuation curves obtained from the Monte Carlo simulations, to be used in shielding calculations. Data for the first exponential are for shallow depth and data for the second exponential are for deep penetration (see text, Section 3.2).

References

[1] M.R. Raju, Heavy Particle Radiotherapy, Academic Press, 1980.
[2] http://ptcog.web.psi.ch/.
[3] E.B. Podgorsak, Radiation Oncology Physics: A Handbook for Teachers and Students, IAEA, 2005.
[4] S. Agosteo, A. Fassò, A. Ferrari, P.R. Sala, M. Silari, P. Tabarelli de Fatis, Double differential distributions and attenuation in concrete for neutrons produced by 100–400 MeV protons on iron and tissue targets, Nuclear Instruments and Methods in Physics Research B 114 (1996) 70–80.
[5] S. Agosteo, M. Magistris, M. Silari, Shielding of proton accelerators, Radiation Protection Dosimetry (2011) 1–11.
[6] E. Mauro, M. Silari, Attenuation of neutrons through ducts and labyrinths, Nuclear Instruments and Methods A 608 (2009) 28–36.
[7] S. Agosteo, M. Magistris, A. Mereghetti, M. Silari, Z. Zajacova, Shielding data for 100–250 MeV proton accelerators: double differential neutron distributions and attenuation in concrete, Nuclear Instruments and Methods in Physics Research B 265 (2007) 581–598.
[8] S. Agosteo, M. Magistris, A. Mereghetti, M. Silari, Z. Zajacova, Shielding data for 100–250 MeV proton accelerators: attenuation of secondary radiation in thick iron and concrete/iron shields, Nuclear Instruments and Methods in Physics Research B 266 (2008) 3406–3416.
[9] S. Agosteo, A. Fassò, A. Ferrari, P.R. Sala, M. Silari, P. Tabarelli de Fatis, Attenuation curves in concrete for neutrons produced by 710 MeV α-particles on steel and water and by 337–390 MeV/u Ne ions on Al, Cu and Pb, Nuclear Instruments and Methods B 155 (1999) 102–109.
[10] S. Agosteo, T. Nakamura, M. Silari, Z. Zajacova, Attenuation curves in concrete of neutrons from 100–400 MeV per nucleon He, C, Ne, Ar, Fe and Xe ions on various targets, Nuclear Instruments and Methods B 217 (2004) 221–236.
[11] S. Agosteo, T. Nakamura, M. Silari, Attenuation curves in concrete of neutrons from 100-400 MeV per nucleon He, C and Ne ions, in: Proceedings of the Sixth Specialists' Meeting on Shielding Aspects of Accelerators, Targets and Irradiation Facilities (SATIF6), NEA/OECD, Stanford (USA), 2004, pp. 65–75. 10-12 April 2002.
[12] S. Agosteo, G. Fehrenbacher, M. Silari, Attenuation curves in concrete of neutrons from 1 GeV/u C and U ions on a Fe target for the shielding design of RIB in-flight facilities, Nuclear Instruments and Methods B 226 (2004) 231–242.
[13] A. Ferrari, P.R. Sala, A. Fassò, J. Ranft, FLUKA: a multi-particle transport code, CERN-2005-10, 2005, INFN/TC_05/11, SLAC-R-773.
[14] G. Battistoni, S. Muraro, P.R. Sala, F. Cerutti, A. Ferrari, S. Roesler, A. Fassò, J. Ranft, The FLUKA code: description and benchmarking, in: M. Albrow, R. Raja (Eds.), Proceedings of the Hadronic Shower Simulation Workshop, Fermilab 6–8 September 2006, AIP Conference Proceeding 896, 2007 pp. 31–49.
[15] S. Agosteo, A. Mereghetti, E. Sagia, M. Silari, Shielding parameters for ion accelerators used in hadron therapy: attenuation of secondary radiation in concrete, Technical Note CERN-RP-2013-052-REPORTS-TN, 2013.
[16] International Commission on Radiological Protection, Conversion Coefficients for Use in Radiological Protection Against External Radiation ICRP Publication 74, Pergamon Press, 1997.
[17] M. Pelliccioni, Overview of fluence-to-effective dose and fluence-to-ambient dose equivalent conversion coefficients for high energy radiation calculated using the FLUKA code, Radiation Protection Dosimetry 88 (2000) 279–297.
[18] J.F. Ziegler, M.D. Ziegler, J.P. Biersack, SRIM – The stopping and range of ions in matter, Nuclear Instruments and Methods in Physics Research B 268 (2010) 1818–1823. http://www.srim.org/.
[19] International Commission on Radiation Units and Measurements, Report No. 33, Bethesda, Maryland, USA, 1980 p. 20.

[20] R.-J. Sheu, Y.-F. Chen, U.-T. Lin, S.-H. Jiang, Deep-penetration calculations in concrete and iron for shielding of proton therapy accelerators, Nuclear Instruments and Methods in Physics Research B 217 (2012) 10–17.
[21] National Council of Radiation Protection, Radiation protection design guidelines for 0.1–100 MeV Particle Accelerators Facilities, NCRP Report 51, 1977.
[22] C. Theis, K.H. Buchegger, M. Brugger, D. Forkel-Wirth, S. Roesler, H. Vincke, Interactive three dimensional visualization and creation of geometries for Monte Carlo calculations, Nuclear Instruments and Methods in Physics Research A 562 (2006) 827–829.
[23] R.H. Thomas, G.R. Stevenson, Radiological safety aspects of the operation of proton accelerators, IAEA Technical Reports Series No. 283, Vienna, 1988.
[24] A. Ferrari, M. Ferrarini, M. Pelliccioni, Secondary particle yields from 400 MeV/u carbon ion and 250 MeV proton beams incident on thick targets, Nuclear Instruments and Methods in Physics Research B 269 (2011) 1474–1481.
[25] A. Porta, S. Agosteo, F. Campi, M. Caresana, Double-differential spectra of secondary particles from hadrons on tissue equivalent targets, Radiation Protection Dosimetry 132 (2008) 29–41.
[26] T. Nakamura, T. Nunomiya, H. Yashima, S. Yonai, Overview of recent experimental works on high energy neutron shielding, Progress in Nuclear Energy 44 (2004) 85–187.
[27] T. Nakamura, L. Heilbronn, Handbook on Secondary Particle Production and Transport by High-Energy Heavy Ions, World Scientific Publ. Co, 2006.
[28] T. Nakamura, Production of neutrons and spallation products by high-energy particle beams, in: Proceedings of the 10th Workshop on Shielding Aspects of Accelerators, Targets and Irradiation Facilities (SATIF10), NEA/OECD, Geneva, Switzerland, 2010, pp. 15–44.
[29] N.V. Mokhov, The Mars Code System User's Guide, Fermilab-FN-628, 1995.